Bioactive Materials 6 (2021) 3125–3135

Contents lists available at ScienceDirect

Bioactive Materials

journal homepage: www.sciencedirect.com/journal/bioactive-materials

Mechanistic insights into the adsorption and bioactivity of fibronectin on surfaces with varying chemistries by a combination of experimental strategies and molecular simulations

Lijing Hao [a,c,d,g,1], Tianjie Li [b,1], Lin Wang [a,f,***], Xuetao Shi [c,f], Yan Fan [c], Chang Du [c,**], Yingjun Wang [d,e,g,*]

[a] School of Materials Science and Engineering, South China University of Technology, Guangzhou, 510640, China
[b] Department of Physics, The Chinese University of Hong Kong, Shatin, N.T., Hong Kong
[c] National Engineering Research Center for Tissue Restoration and Reconstruction, Guangzhou, 510006, China
[d] Key Laboratory of Biomedical Engineering of Guangdong Province, Guangzhou, 510006, China
[e] Key Laboratory of Biomedical Materials and Engineering of the Ministry of Education, Guangzhou, 510006, China
[f] Innovation Center for Tissue Restoration and Reconstruction, Guangzhou, 510006, China
[g] Bioland Laboratory (Guangzhou Regenerative Medicine and Health Guangdong Laboratory), Guangzhou, 510005, China

ARTICLE INFO

Keywords:
Fibronectin
Self-assembled
hBMSCs
Molecular dynamics simulation
Orientation

ABSTRACT

Fibronectin (Fn) is significant to the performance of biomaterials, and the chemistry of biomaterial surface play important roles in Fn adsorption and subsequent cell behavior. However, the "molecular scale" mechanism is still unclear. Herein, we combined experimental strategies with molecular simulations to solve this problem. We prepared self-assembled monolayers with varying chemistries, i.e., SAMs-CH_3, SAMs-NH_2, SAMs-COOH and SAMs-OH, and characterized Fn adsorption and cell behaviors on them. Next, Monte Carlo method and all-atom molecular dynamics simulations were employed to reveal the orientation/conformation of Fn on surfaces. We found that SAMs-CH_3 strongly adsorbed Fn via hydrophobic interactions, but show poor bioactivity as the low exposure of RGD/PHSRN motifs and the deformation of Fn. SAMs-NH_2 and SAMs-COOH could adsorb Fn efficiently via vdW interactions, electrostatic interactions, hydrogen bonds and salt bridges. Fn exhibited excellent bioactivity for cell adhesion, proliferation and osteogenic differentiation as high exposure of bioactive motifs on SAMs-NH_2, or as the activation of other inferior cell-binding motifs on SAMs-COOH. SAMs-OH showed poor Fn adsorption as the water film. However, the adsorbed Fn displayed non-negligible bioactivity due to high exposure of PHSRN motif and large degree of protein flexibility. We believe that the revealed mechanism presents great potential to rationally design Fn-activating biomaterials.

1. Introduction

After implantation, the performance of biomaterials is mainly determined by the proteins they have adsorbed, as these proteins are the bridges between the cells and the biomaterial; i.e., cells adhere to the biomaterials via these proteins [1]. Among the adsorbed proteins, those in the integrin family are of great significance due to their excellent bioactivity to modulate cell fate [2]. In particular, the integrin fibronectin (Fn) has attracted much attention [3,4]. As previously reported, Fn can bind many important biomolecules, e.g., collagen [5], fibrin [6] and a variety of growth factors [7], to undergo fibrillogenesis and influence essential cellular processes [8]. Additionally, there are PHSRN and RGD motifs in Fn, both of which play a significant role in the bioactivity of Fn [7].

After adsorption onto the biomaterial surface, the controllable conformations of these proteins are extremely important for exhibition of

Peer review under responsibility of KeAi Communications Co., Ltd.
* Corresponding author. Key Laboratory of Biomedical Engineering of Guangdong Province, Guangzhou, 510006, China.
** Corresponding author. National Engineering Research Center for Tissue Restoration and Reconstruction, Guangzhou 510006, China.
*** Corresponding author. School of Materials Science and Engineering, South China University of Technology, Guangzhou, 510640, China.
E-mail addresses: wanglin3@scut.edu.cn (L. Wang), duchang@scut.edu.cn (C. Du), imwangyj@scut.edu.cn (Y. Wang).
[1] These authors contributed equally to this work.

https://doi.org/10.1016/j.bioactmat.2021.02.021
Received 16 October 2020; Received in revised form 2 February 2021; Accepted 17 February 2021
Available online 9 March 2021

their bioactivity [9]. Fn can participate in physiological processes only when it is in its ordered conformation, exposing the abovementioned bioactive motifs [10]. Therefore, modifying the biomaterial surface with controllable Fn adsorption is a widely acceptable strategy for the rational design and development of novel Fn-activating biomaterials [11]. Common strategies for creating an Fn-activating biomaterials include modulating the morphology [12], chemistry [13], surface energy [14] or composition of the biomaterial surface [15], which have profound consequences on the regulation of Fn adsorption and further improvements in cell adhesion, proliferation and differentiation.

Among these strategies, modulating the chemical groups on the biomaterial surface has become significant, as this method strongly regulates Fn adsorption by affecting the chemical composition, hydrophilicity and charge of the surface [16]. Studies have modified biomaterial surfaces with a variety of chemical groups, e.g., oligoethylene glycol (-OEG) [17], $–CH_3$ [18], $-PO_3H_2$ [19], $–NH_2$ [20], –COOH [13] or –OH [21]' and evaluated their effects on Fn adsorption and cell behavior. To mechanistically reveal the relationship between these biomaterial surfaces and the conformation/bioactivity of Fn at the molecular scale, Monte Carlo (MC) or molecular dynamics (MD) simulations are often employed [22,23]. However, during these simulations, the length of simulation periods and the simulation methodologies still need to be improved to eliminate the mismatching between simulations and reality. Moreover, the closer combination of simulations and experimental strategies is urgently required. These facts have become very large obstacles for the rational design of Fn-activating biomaterials that are in high demand in the clinic.

In the present study, we combined experimental strategies, Monte Carlo and all-atom MD simulations to overcome this critical and overlooked long-lasting problem of "chemistry-conformation-bioactivity". We prepared self-assembled monolayers (SAMs) on gold containing methyl ($-CH_3$), amino ($-NH_2$), carboxyl (-COOH) and hydroxyl (-OH) groups to mimic biomaterial surfaces with different chemical groups. Then, we employed the experimental strategy of surface plasmon resonance (SPR) to characterize the binding behaviors of Fn on the surfaces of the biomaterials, including adsorption rate, binding capacity and binding kinetics. We characterized the biocompatibilities and osteogenic activities of Fn on these surfaces to *human bone marrow mesenchymal stem cells* (*hBMSCs*). Finally, we employed the Monte Carlo method and all-atom MD simulations to reveal the molecular-scale mechanism of the difference in adsorption and bioactivity of Fn on the SAM substrates and demonstrated that there was a close connection between the orientation/conformation of Fn and its adsorption/bioactivity. These findings will be of great significance for the rational design and development of Fn-activating biomaterials.

2. Materials and methods

2.1. Surface preparation

Gold substrates were prepared by coating titanium (10 nm) and gold (40 nm) layers onto silicon wafers using an ANELVA L-400EK electron beam evaporator (Canon Anelva Corporation, Kanagawa, Japan) and then diced into pieces (10 mm × 10 mm × 1 mm) with a DS820 automatic dicing saw. Then, the gold substrates were cleaned via nitrogen plasma treatment for 2 min with an HPC plasma cleaner system. Next, the substrates were washed with ethanol and highly purified water for 3 times, and dried with a stream of nitrogen gas. The freshly cleaned gold slides were immediately immersed in 1 mL of alkanethiol (1-dodecanethiol ($CH_3(CH_2)_{10}CH_2SH$, ≥98%, Sigma-Aldrich, USA), 11-amino-1-undecanethiol, hydrochloride ($HS(CH_2)_{11}NH_2HCl$, ≥90%, Dojindo, Japan), 10-carboxy-1-decanethiol ($HS(CH_2)_{10}COOH$, ≥97%, Dojindo, Japan) or 11-mercapto-1-undecanol ($HSCH_2(CH_2)_9CH_2OH$, 99%, Sigma-Aldrich, USA)) in ethanol (1 mM) for 24 h at room temperature. After incubation, the samples were washed by ethanol and highly purified water. Then, SAMs with four chemical groups ($-CH_3$, $–NH_2$, –COOH and –OH) were obtained and referred to as SAMs-CH_3, SAMs-NH_2, SAMs-COOH and SAMs-OH, respectively.

2.2. Fn adsorption

All SAM substrates were immersed in 20 μg mL^{-1} Fibronectin (Fn, R&D Systems, USA) solution in phosphate buffered saline (PBS, Gibco, USA) and incubated at 37 °C in a humidified incubator with 5% CO_2 for 1 h. Then, the Fn-coated surface was characterized by X-ray photoelectron spectroscopy (XPS, AXIS-ULTRADLD, KRATOS, UK) and atomic force microscopy (AFM, MFP-3D-S, Asylum Research, USA).

The adsorption kinetics of various concentrations of Fn (1, 5, 10, 20 and 40 μg mL^{-1}) on SAM surfaces were determined with a Plexera Kx5 V2 SPRi apparatus (Plexera® Bioscience LLC, USA). Briefly, the SAMs were prepared on the SPR sensor (25 mm × 75 mm × 1 mm) surface by immersing it in 12.5 mL of the reaction solution (1 mM) for 24 h at room temperature, and washed by ethanol and highly purified water. Then, PBS was introduced into the SPR liquid cell for the baseline, and Fn solutions at different concentrations in PBS were injected at a rate of 2 μL s^{-1}. The raw sensorgram data (expressed as refractive units, RU) and the kinetic binding constants from SPR were analyzed by PlexeraDE.exe Software, and the mass of Fn on the SAM surface was calculated (1000 RU corresponds to a protein density of 1 ng mm^{-2}).

To evaluate the activity of Fn, the surfaces with Fn were blocked with 3% Bovine Serum Albumin (BSA, Thermoscientific, USA) and then incubated with complete medium at 37 °C for 1 h. After that, the activity of Fn on the surface was determined by an enzyme-linked immunosorbent assay (ELISA) (Quantikine® ELISA) with a monoclonal antibody (mAb) (HFN7.1, R&D Systems, USA) directed toward the epitopes of the RGD-containing domains according to the manufacturer's instructions.

2.3. In vitro cell assay

Human bone marrow mesenchymal stem cells (*hBMSCs*) (Cyagen Biosciences Inc., USA) were cultured in culture medium (Cyagen Biosciences Inc., USA) containing 10% fetal bovine serum (FBS, Cyagen Biosciences Inc., USA). The medium was changed every two days, and cells in the early passages (≤6) were collected for the *in vitro* assay. Before cell seeding, the SAM substrates were immersed in 20 μg mL^{-1} Fn solution and incubated for 1 h (37 °C, 5% CO_2). Then, the samples were further blocked with nonadhesive BSA (3% w/v) for 1 h (37 °C, 5% CO_2) to prevent the adsorption of additional proteins that may influence cell activity.

2.3.1. Cell adhesion and proliferation

To characterize cell adhesion on the substrates, cells (5×10^4 cells per sample) were seeded onto SAM substrates containing adsorbed Fn and cultured for 12 h. Then, the samples were fixed in 4% formaldehyde for 30 min and permeabilized with 0.1% Triton X-100 PBS for 10 min. The cells were stained with F-actin (Alexa Fluor® 555, ThermoFisher Scientific, USA) for 20 min followed by DAPI (Beyotime, China) for 5 min and observed by confocal laser scanning microscopy (CLSM, Leica TCS SP5, Germany).

For the cell proliferation assay, cells (1×10^4 cells per sample) were seeded onto SAM substrates containing adsorbed Fn for 1, 3 and 5 days of culture. Then, the samples were transferred to a new plate, and cell viability was evaluated by a Cell Counting Kit-8 (CCK-8, Dojindo, Japan) assay by immersing the samples into 300 μL of the CCK-8 working solution for 1 h of incubation. The absorbance at 450 nm was measured with a microplate reader (Thermo3001, USA). Additionally, we calculated the cellular proliferation rates based on CCK-8 results by the slopes of the quadratic fitting equation as follows:

$$y = A_1x^2 + B_1$$

After 12 h of culture in growth medium, the gene expression and

protein expression of integrin β_1 were measured by the qRT-PCR assay and Western blot, respectively. The total RNA was isolated by HiPure Total RNA Kits (Magentec, China) and then reverse transcribed into cDNA using the PrimeScript® RT reagent Kit with gDNA Eraser (TaKaRa Biotechnology, Japan) according to the manufacturer's protocol. The total protein was extracted using lysis buffer (KeyGEN BioTECH, China) and then concentrated by centrifugation. The concentration of the supernatant was determined by a BCA™ Protein Assay Kit (KeyGEN BioTECH, China) and then separated with a SDS-PAGE gel electrophoresis kit (KeyGEN BioTECH, China). The protein expression of integrin β_1 was analyzed by Western blot utilizing primary antibodies against β_1 (1:20,000, Abcam, UK). The dilutions used of the secondary antibody were 1:5000.

2.3.2. Osteogenic differentiation

For the qRT-PCR assay, cells (5×10^4 cells per sample) were cultured on the SAM samples in osteogenic differentiation medium (Cyagen Biosciences Inc., USA). After 7 and 14 days of culture, the total RNA was isolated and then reverse transcribed into cDNA as described above. Then, qRT-PCR was performed using the SYBR Green system (Invitrogen, USA). Briefly, the samples were held at 95 °C for 10 min, followed by 40 cycles at 95 °C for 15 s and 60 °C for 1 min. The relative quantification of the target genes was analyzed by the $2^{-\Delta\Delta Ct}$ method. The primers and probe sequences (TaKaRa Biotechnology, Japan) are shown in Table S1.

After 7 days of culture in osteogenic differentiation medium, ALP staining was conducted following the manufacturer's instructions using the BCIP/NBT phosphatase substrate (1-Component) (KPL, USA). The stained surface was observed by a digital three-dimensional video microscope (HIROX KH-7700, Japan).

The matrix mineralization of the cells on the SAM substrates were assessed for calcium deposits by Alizarin Red (AR) staining (KGA363, KeyGEN BioTECH, China). Briefly, after 14 days of culture in osteogenic differentiation medium, the samples were fixed in 4% formaldehyde, immersed in 500 μL of the working solution and further incubated for 0.5 h. Next, the samples were washed with highly purified water. The stained surfaces were observed with a digital three-dimensional video microscope (HIROX KH-7700, Japan). Then, the stained cells were eluted by cetylpyridinium chloride (CPC, Aladdin®, China) at a concentration of 10% (w/v), and the absorbance at 550 nm was measured with a microplate reader (Thermo3001, USA).

2.4. Molecular simulations

2.4.1. System construction

Computational structures of SAMs containing the four chemical groups (-CH_3, –NH_2, –COOH and –OH) were modeled with the corresponding alkanethiol molecules in the experiments. Each SAM consisted of 396 alkanethiol chains. Thirty chains on SAMs-COOH were chosen randomly to be protonated with a surface charge density of 0.05 C m^{-2}, which corresponded to that of SAMs-NH_2 (−0.05 C m^{-2}). The 7th-10th type-III domains of Fn (Fn-$III_{7\text{-}10}$, PDB: 1FNF) containing the PHSRN synergy peptide on Fn-III_9, and the RGD motif on Fn-III_{10} was chosen as an appropriate alternative for full-length Fn in the simulation, holding a net charge of −14 and having 7 β-strands that form two antiparallel β-sheet layers (Fig. 1).

2.4.2. Monte Carlo (MC) method

MC calculations were conducted to provide optimized orientations of the protein for initiating MD simulations. SAMs surfaces were simplified into endless planes with corresponding surface charge densities, and Fn-$III_{7\text{-}10}$ was simplified into a coarse-grained α-carbon model that remained rigid throughout the calculation. Fn-$III_{7\text{-}10}$ was placed over the endless plane by 10 nm. Electrostatic and van der Waals interactions were calculated with empirical equations and the corresponding parameters according to other works [24,25]. A total of 80,000,000 MC circulations were carried out by transferring and rotating Fn-$III_{7\text{-}10}$ around the center of mass. The first 40 million was performed for equilibration, while the rest were employed for statistical analysis.

2.4.3. All-atom MD simulation protocols

All-atom MD simulations of Fn-$III_{7\text{-}10}$ were carried out using GROMACS 5.1.5 [26] with the CHARMM36 and CHARMM General force field [27,28]. The parameters of the SAMs were derived from the CHARMM General force field [27,29]. All SAM sulfur atoms were kept stationary during the MD simulations. Approximately 70,000 water molecules described by the TIP3P model [30] were added to a rectangular box with dimensions of 18.000 nm × 9.526 nm × 15.000 nm. Chloride and sodium ions were added to neutralize the system charge and imitate physiological ionic concentration. Fn-$III_{7\text{-}10}$ was placed 0.5 nm above the SAMs with the optimized orientations from the MC results.

Simulations were performed in a canonical ensemble with a time step of 2 fs, and the system temperature was controlled at 300 K by a Nosé-Hoover thermostat [31] using a coupling time of 0.5 ps. The initial velocity of each atom was assigned from a Maxwell-Boltzmann distribution at 300 K. All hydrogen bonds were constrained by the LINCS algorithm [32]. Nonbonded interactions were calculated by a switch function that started at 9 Å and cut off at 12 Å. Electrostatic interactions were calculated by the particle mesh Ewald (PME) method [33] in 3dc geometry with a cutoff distance of 12 Å. Periodic boundary conditions were applied only in the x and y directions. Two hard walls were set at the top and bottom sides of the simulation box. The systems were subjected to energy minimization using the steepest descent method to eliminate steric overlap or inappropriate geometry, followed by a 100 ps NVT equilibration with position restraints on the heavy atoms of the protein backbone. Afterwards, a 300 ns production simulation was

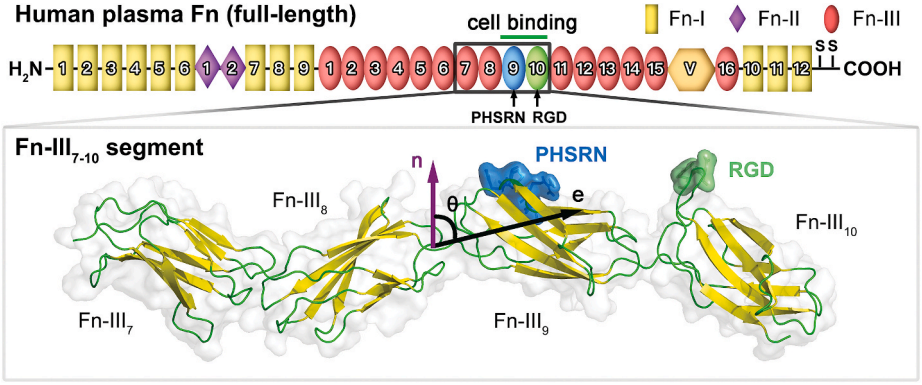

Fig. 1. Functional domains of human-derived plasma Fn and the crystal structure of the Fn-$III_{7\text{-}10}$ segment. The orientation of Fn-$III_{7\text{-}10}$ is quantified by the angle (θ) between the normal vector **n** and its electric dipole moment **e**.

performed for each system. Calculations for the orientation angle and gyrate radius of Fn-III$_{7\text{-}10}$, and the solvent accessible surface area (SASA) of both cell-binding sites were implemented with GROMCAS package. Meanwhile, the root-mean-square deviation (RMSD), interdomain angle, distance between protein structural elements and SAMs, and intermolecular polar interactions (hydrogen bonds and salt bridges) were measured by VMD-1.9.4 [34]. Clustering analyses were conducted for the last 100 ns by calculating the backbone rmsd in pairs using GROMACS, and only the centroid structure of top cluster was presented as the representative adsorption state in this paper. The intermolecular free energies between Fn and the SAMs were calculated using the g_mmpbsa tool [35,36]. VMD-1.9.4 [34] and PyMOL-2.2.4 [37] were both used for visualization. The secondary structure of Fn-III$_{7\text{-}10}$ was measured by the DSSP tool [38,39].

2.5. Contour mapping

A 20 × 20 data matrix was generated by interpolation using Kriging correlation method from the raw data set. Briefly, the iso-electric point (charge) and water contact angle (hydrophobicity) of SAMs surface were obtained by experiment and taken as independent variables. Then, adsorption amount, proliferation rates and gene expressions of *hBMSCs*, and SASA of the bioactive sequences were mapped.

2.6. Statistical analysis

Statistical comparison was determined by analysis of variance (ANOVA) followed by post-hoc test and a $p < 0.05$ was considered to be statistically significant.

3. Results and discussion

3.1. Fn adsorption onto SAMs

We successfully prepared SAMs with four functional end groups, i.e., –CH_3, –NH_2, –COOH and –OH, by self-assembly onto gold substrates. As reported, these groups could represent a hydrophobic (SAMs-CH_3) and hydrophilic (SAMs-NH_2, SAMs-COOH and SAMs-OH) surfaces as well as neutral (SAMs-CH_3 and SAMs-OH), positively charged (SAMs-NH_2) and negatively charged (SAMs-COOH) surfaces [20]. A detailed characterization of these SAMs selected for this work has been published in our previous study, demonstrating that surface chemistry from wettability to charge directed *BMSCs* fate [40–42]. The previous results demonstrated that SAMs-CH_3 were hydrophobic with a water contact angle of 112.58 ± 1.56°, while SAMs-NH_2, SAMs-COOH and SAMs-OH were hydrophilic with water contact angles of 68.38 ± 2.01°, 38.8 ± 2.86° and 22.18 ± 1.63°, respectively [42]. The zeta potential results from SAMs-CH_3, SAMs-NH_2, SAMs-COOH and SAMs-OH are shown in other references, with isoelectric points of 3.2, 6.2, 2.8 and 4.0, respectively [42].

Fn could adsorb onto the SAM substrates but showed very different adsorption capabilities depending on the particular substrate. The XPS N1s high-resolution spectrum showed that before adsorption, there were negligible N1s signals from SAMs-CH_3, SAMs-COOH and SAMs-OH, while a weak N1s signal was detected from SAMs-NH_2 due to the amino group (Fig. 2A). Notably, after treatment with the Fn solution, strong N1s signals were detected from these four SAM substrates (Fig. 2A), demonstrating successful Fn adsorption. Interestingly, the N1s signals from SAMs-CH_3, SAMs-NH_2 and SAMs-COOH were much stronger than those from SAMs-OH, showing the lower adsorption of Fn onto SAMs-OH. The AFM results showed that after the adsorption of Fn, the identity of the chemical group made a big difference on the surface morphology (Fig. S1). Different from the Fn on SAMs-NH_2 and SAMs-COOH, which exhibited dot-like distributions, the Fn on SAMs-CH_3 had a mesh structure with nanocavities. As reported, conformational rearrangement is usually necessary for a protein to obtain an equilibrium adsorption state on hydrophobic surfaces [43], which would lead to the mesh structure of Fn on SAMs-CH_3. Additionally, the Fn on SAMs-OH displayed a smooth morphology.

We quantitatively analyzed Fn adsorption by SPR. The results showed that after Fn injection at concentrations ranging from 1 to 40 μg mL^{-1}, the protein could immediately adsorb onto SAMs-CH_3, SAMs-NH_2 and SAMs-COOH, and rapidly reach saturation with the fast increase in the SPR response (Fig. 2B). After being washed with PBS and according to the procedure [44], the densities of Fn on these three SAM substrates with 20 μg mL^{-1} Fn solution were 1.376, 0.985, and 1.368 ng mm^{-2}, respectively (Fig. 2C). However, the density of Fn was only 0.009 ng mm^{-2} on SAMs-OH after washing (Fig. 2C). These results were consistent with the XPS results (Fig. 2A) that Fn was difficult to adsorb onto

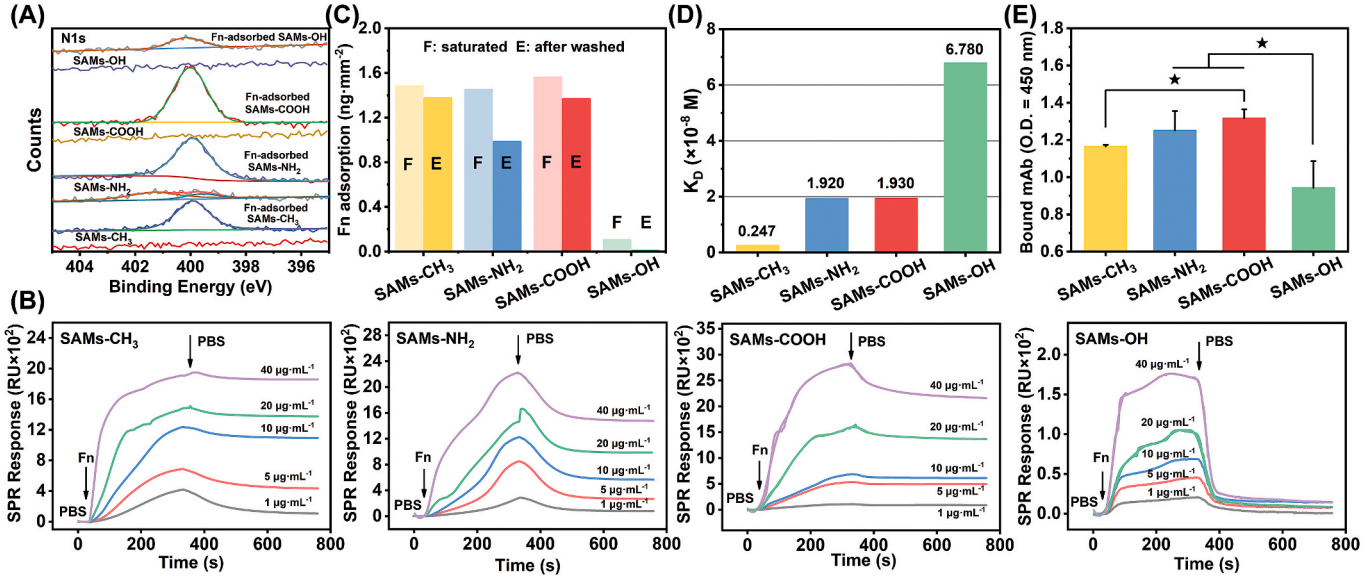

Fig. 2. Characterization of Fn adsorption on SAM substrates. (A) XPS N1s high-resolution spectra of the samples before and after Fn adsorption. (B) Real-time SPR sensorgrams of Fn adsorption on the indicated SAM substrates. (C) The saturated and final adsorption mass on the indicated substrates with 20 μg mL^{-1} Fn solution. The mass was calculated according to the SPR response, in which 1000 RU corresponded to a protein density of 1 ng mm^{-2}. (D) The dissociation constant (K_D) for Fn adsorption calculated from the SPR results. (E) ELISA for the bioactivity of Fn on the indicated surfaces (n = 5).

SAMs-OH. We further employed the kinetic rate constants (K_D values) of dynamic adsorption and desorption to quantify the binding of Fn on the SAM substrates (Fig. 2D). The results showed that SAMs-CH_3 had the lowest K_D value with the fastest adsorption reaction. As the neutral surface, being different from SAMs-CH_3, SAMs-OH displayed the fastest desorption reaction with a much higher K_D value than those of the other groups. Additionally, although there was less Fn on SAMs-NH_2 than those on SAMs-COOH, their K_D values showed negligible difference.

We further employed ELISA to characterize the exposure of the cell-binding domains on the adsorbed Fn. The results showed that although there was more Fn on SAMs-CH_3 than on the other three surfaces, its bound mAbs in unit mass was much lower, leading to the lower total bound mAbs than SAMs-NH_2 and SAMs-COOH (Fig. 2E and Fig. S2). This result illustrated that Fn would shield more active domains on SAMs-CH_3, further impacting the bioactivity of the protein. Notably, although there were less Fn adsorbed on SAMs-OH and its total bound mAbs was lowest (Fig. 2E), the bound mAbs in unit mass was highest (Fig. S2), indicating the non-negligible bioactivity of Fn on SAMs-OH. Meanwhile, the Fn on SAMs-NH_2 and SAMs-COOH exhibited high total bound mAbs, demonstrating that these two surfaces could both absorb Fn and maintain its bioactivity (Fig. 2E).

3.2. *In vitro* cell assay

We further employed an *in vitro* cell assay to verify the bioactivities of Fn on different SAM substrates. All substrates for the cell assay were incubated in Fn solution (20 μg mL^{-1} in PBS) at 37 °C with 5% CO_2 for 1 h. The fluorescent images showed that the cells on SAMs-NH_2, SAMs-COOH and SAMs-OH with Fn displayed a well-spread morphology, while those cells on SAMs-CH_3 with Fn had an elongated status, demonstrating poor adhesion (Fig. 3A). The CCK-8 results showed that after 1, 3 and 5 days of culture, the cells on SAMs-NH_2 and SAMs-COOH with Fn exhibited excellent proliferation, demonstrating the high bioactivity of Fn on these surfaces (Fig. 3B). Meanwhile, the rate of proliferation on SAMs-NH_2 was the highest (Fig. 3B and Fig. S3). However, the cells showed negligible proliferation on SAMs-CH_3 with Fn. For example, after 5 days of culture, the cell viability on SAMs-CH_3 with Fn was only 0.51-, 0.58- and 0.60-fold compared to that on SAMs-NH_2, SAMs-COOH and SAMs-OH with Fn, respectively (Fig. 3B). This result demonstrated the poor bioactivity of the protein on SAMs-CH_3. Additionally, although there were much less Fn on SAMs-OH, the cells on it showed good proliferation, i.e., a little lower than SAMs-NH_2 and SAMs-COOH, but much higher than SAMs-CH_3. This result demonstrated that the Fn on SAMs-OH displayed non-negligible bioactivity.

We found that Fn on the SAMs surfaces exhibited the above enhancement in adhesion and proliferation by strongly promoting the expression of integrin β_1 in cells at both the gene and protein levels. As previously reported, integrins are a large family of cell surface receptors that mediate cell-extracellular matrix interactions as well as intercellular interactions [45]. Expression of integrin β_1 enables cells to bind to

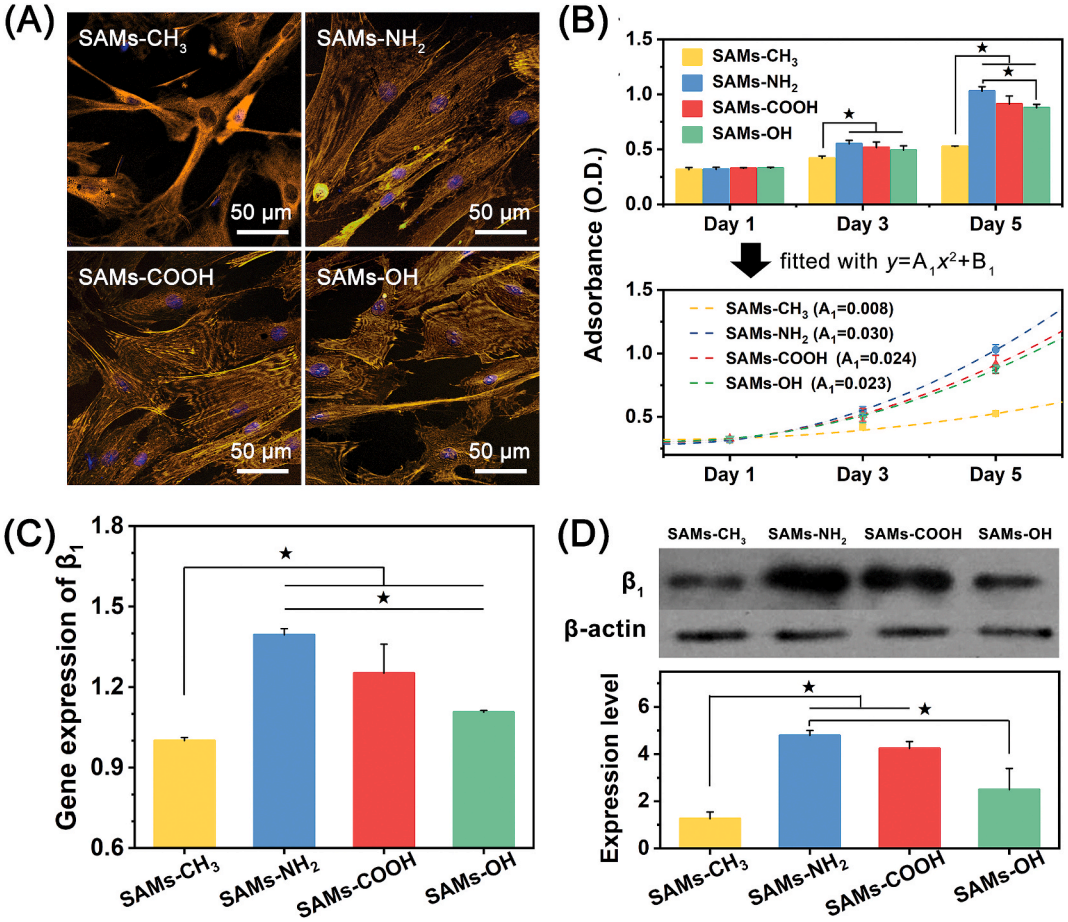

Fig. 3. *In vitro* cell adhesion and proliferation assay on SAM substrates with Fn. (A) The morphologies of the cells after 12 h of culture on the indicated surfaces. The cells were stained with F-actin (Alexa Fluor® 555) and DAPI, in which the cell cytoskeleton was orange and the nuclei were blue. (B) CCK-8 assay for the proliferation of the cells on the indicated surfaces after 1, 3 and 5 days of culture (n = 5). The data was fitted with a quadratic equation and then the proliferation rate was obtained from the slope ($\mathbf{A_1}$). (C) qRT-PCR assay for the gene expression of integrin β_1 in the cells on the indicated surfaces after 12 h of culture (n = 4). (D) Western blot results and the quantitative assay for the protein expression of integrin β_1 in the cells on the indicated surfaces after 12 h of culture (n = 4). ★ denotes $p < 0.05$.

extracellular matrix proteins, trigger intracellular signals with the actin cytoskeleton and enter the mitotic cycle. The qRT-PCR results and Western blot results showed that the cells on SAMs-NH_2 with Fn exhibited the highest gene and protein expression of integrin β_1, showing 1.40-, 1.11- and 1.26-fold higher gene expression and 3.81-, 1.13-, 1.92-fold higher protein expression compared to SAMs-CH_3, SAMs-COOH and SAMs-OH, respectively (Fig. 3C and D). Moreover, the lowest expression of integrin β_1 was observed on SAMs-CH_3, which was consistent with the adhesion and proliferation results (Fig. 3A and B).

Furthermore, we demonstrated that Fn on the SAM surfaces showed different osteogenic activities. After 7 and 14 days of culture, Fn on SAMs-CH_3 showed lower osteogenic activity to *hBMSCs* due to the poor bioactivity. Conversely, Fn on SAMs-NH_2 and SAMs-COOH could up-regulate the expression of osteogenic genes in hBMSCs, i.e., OC on the 7th day, OC and Col-I on the 14th day, compared with the expression on SAMs-CH_3 (Fig. 4A). The results of Alizarin red (AR) staining and ALP staining showed a similar trend to the qRT-PCR results (Fig. 4B, C and Fig. S4). Specifically, after 14 days of culture and AR staining, more red-formazan areas were found on SAMs-NH_2 and SAMs-COOH (Fig. 4B). Quantitative analysis showed that the OD value of SAMs-COOH was higher than that of SAMs-NH_2, while these two surfaces were 1.25- and 1.12-fold compared to SAMs-CH_3, respectively (Fig. 4C). And these results were consistent with that hBMSCs on SAMs-NH_2 and SAMs-COOH had higher expressions of integrin β_1. Interestingly, Fn on SAMs-OH showed lower osteogenic activity to *hBMSCs*, being similar to those on SAMs-CH_3 (Fig. 4A–C) and inconsistent with the proliferation results. The inconsistency of proliferation and differentiation was also observed in other references. It was because that these two behaviors were different biological processes [13,46–48], and the cell differentiation would be determined by the comprehensive functions of several parameters [41,49,50]. The above results demonstrated that the Fn on SAMs-NH_2 and SAMs-COOH had higher osteogenic activity than Fn on the other surfaces.

3.3. Molecular simulations

As reported, SAM substrates with different chemical groups affect the adsorption and bioactivity of Fn. Our research further showed that Fn strongly adsorbed on SAMs-CH_3, SAMs-NH_2 and SAMs-COOH but encountered more difficulty adsorbing onto SAMs-OH. Additionally, the *in vitro* cell assay demonstrated that the Fn on SAMs-NH_2 and SAMs-COOH had higher bioactivity. However, the "molecular-scale" mechanism of the above phenomenon is still unclear, which hampers the development of Fn-activating biomaterials.

In the present study, we employed molecular simulations to reveal the mechanism of the difference in Fn adsorption and bioactivity on these SAM substrates. We chose Fn-$III_{7\text{-}10}$ as an appropriate alternative for the full-length Fn segment in the molecular simulation, as this segment has been confirmed to retain the ability of full-length Fn to mediate cell adhesion [16]. After MC optimization, five orientations were obtained statistically: O_1, O_2 and O_2' for the surface with neutral charge (SAMs-CH_3 and SAMs-OH), O_3 for the surface with positive charge (SAMs-NH_2) and O_4 for the surface with negative charge (SAMs-COOH) (Fig. 5A and B). These optimized orientations were placed above the corresponding SAMs to initiate the subsequent all-atom MD simulations. Notably, O_2 and O_2' demonstrated equivalent binding orientations where Fn-III_8 was bound to the substrate, but O_2 was selected due to its higher contact area with the substrate.

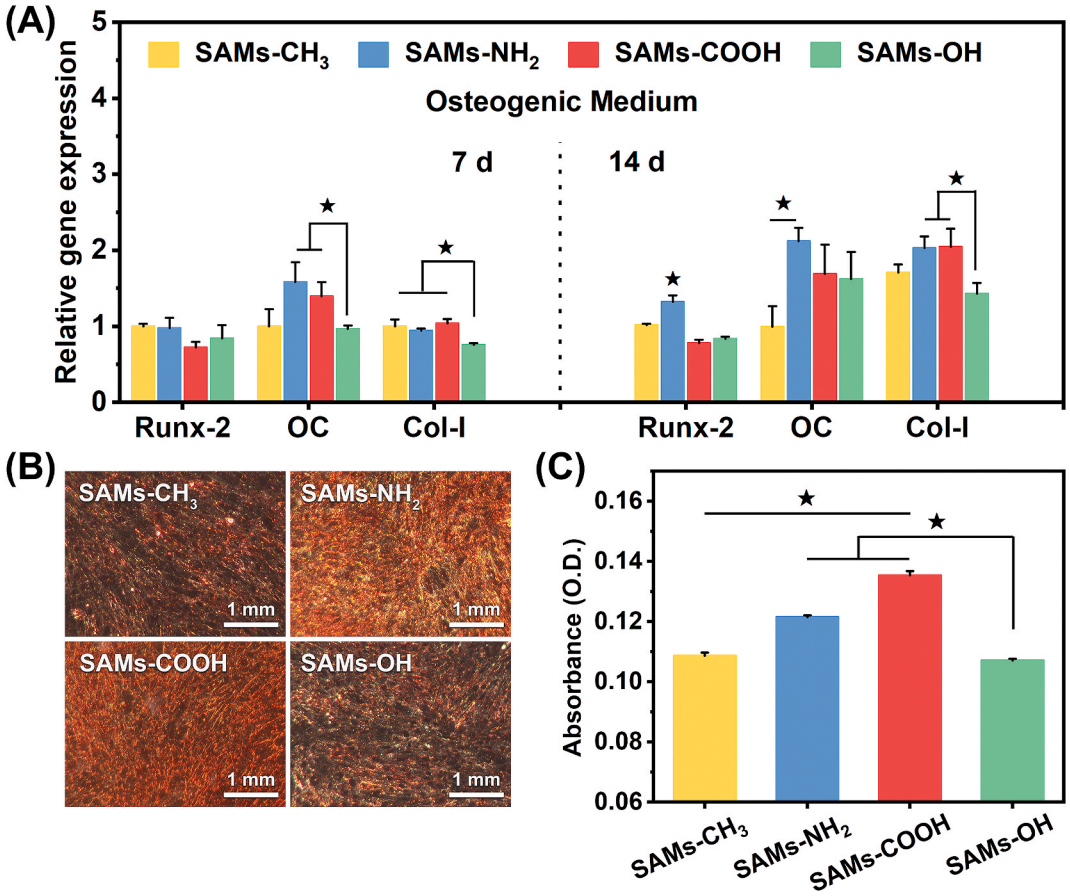

Fig. 4. ***In vitro*** **osteogenic differentiation of** ***hBMSCs*** **on the indicated surfaces with Fn.** (A) qRT-PCR assay for the gene expression of Runx-2, OC and Col-I in the cells on the indicated surfaces after 7 and 14 days of culture (n = 4). (B) and (C) Alizarin red (AR) staining and quantitative analysis of the cells on the indicated surfaces after 14 days of culture (n = 6), respectively. ★ denotes $p < 0.05$.

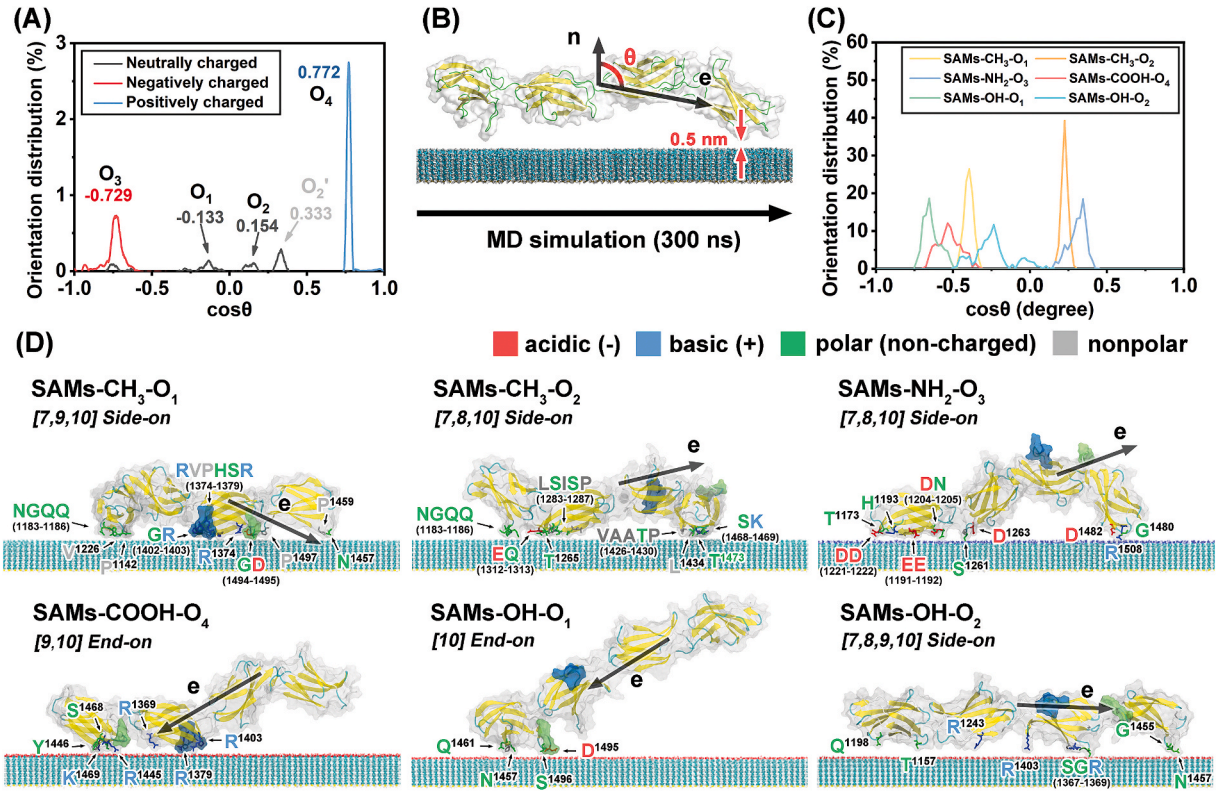

Fig. 5. Binding of Fn-III$_{7\text{-}10}$ to SAMs in simulations. (A) The orientations of Fn-III$_{7\text{-}10}$ on the indicated surfaces after MC optimization. (B) The initial structure of Fn for MD simulations. Fn-III$_{7\text{-}10}$ was placed 0.5 nm over the SAMs with a defined orientation angle (θ) obtained from MC optimization. (C) The orientations of Fn-III$_{7\text{-}10}$ on the indicated surfaces during MD simulations. 300 ns MD simulation was performed, and the data of the last 100 ns were extracted for analysis. (D) The orientation distributions of Fn-III$_{7\text{-}10}$ on the indicated surfaces in MD simulations. The protein residues close to the SAMs (distance ≤ 3.5 Å) were shown and labeled on the side in specific colors according to the type of side chain. Domains bound to the SAMs are listed in the square bracket followed by the type of orientation. **e** represents the electric dipole moment of Fn-III$_{7\text{-}10}$. The RGD and PHSRN motifs are shown in lime and blue transparent surface representation, respectively.

After 300 ns of simulation, the frames from the last 100 ns of trajectories were extracted for analysis, as the protein came to a relatively stable binding structure deduced from the low fluctuations in RMSD during this period (Fig. S5). We found that in this period, Fn showed "side-on" or "end-on" orientations on different SAM substrates (Fig. 5C and D), while the binding domains were labeled according to the minimum distance between each domain and the SAMs substrate (Fig. S6). On SAMs-CH_3 and SAMs-NH_2, Fn exhibited a "side-on" orientation to bind to the SAM surface, in which at least three domains, especially both the end domains (Fn-III$_7$ and Fn-III$_{10}$), bound to the SAMs surface (Fig. 5D and Fig. S6). However, the "end-on" orientation was observed on SAMs-COOH, in which only Fn-III$_9$ and Fn-III$_{10}$ bound to the SAM surface (Fig. 5D and Fig. S6). Interestingly, there were both "side-on" and "end-on" orientations on SAMs-OH, and neither orientation was stable with changing values of orientation angle (Fig. 5C and Fig. S6). This result demonstrated that Fn had weak adsorption and was not stable on SAMs-OH, which was consistent with the XPS and SPR results (Fig. 2).

We investigated the interactions between Fn-III$_{7\text{-}10}$ and SAMs with neutral charge, i.e., SAMs-CH_3 and SAMs-OH, from the last 100 ns of the MD simulations (Fig. 6). The results showed that there were vdW interactions and electrostatic interactions appearing in similar proportions between Fn and SAMs-CH_3, but negligible intermolecular polar interaction was observed (Fig. 6A and B). By further analysis of the average distance between protein residues and SAMs-CH_3 (Fig. S7), we found that Fn adsorbed onto SAMs-CH_3 via main interactions of both the side chains of nonpolar amino acids, e.g. Pro^{1142}, Val^{1226}, Pro^{1227}, Pro^{1287}, Pro^{1376}, Val^{1426}, Ala^{1427}, Pro^{1430}, Leu^{1434}, Pro^{1459}, and Pro^{1497}, and the methylene parts on the side chains of lysine or arginine, e.g. Lys^{1223}, Arg^{1369}, Arg^{1374}, Arg^{1379}, Arg^{1403}, and Lys^{1469} (Fig. 5D and Fig. S7), indicating the strong hydrophobic interactions between Fn and the surface. Interestingly, there was a hydrophilic loop bulging on the surface of Fn-III$_7$ (NGQQ) that bound to SAMs-CH_3. This binding was likely retained by the local entropy-driven hydrophobic interaction between SAMs-CH_3 surface and the methylene groups of asparagine and glutamine/the α-hydrogen of glycine. Due to the less directionality of strong hydrophobic interaction, the bound Fn was endowed with high mobility along the SAMs-CH_3 substrate and tended to aggregate into a compact layer, resulting in the highest density and the lowest K_D value (Fig. 2). Being different from the Fn adsorption on hydrophobic surface, there was a water film between the protein and the hydrophilic substrates (SAMs-COOH, SAMs-NH_2 and SAMs-OH), which could be quantified by the intermolecular polar solvation energies (Fig. 6B). The water film promoted the prior formation of hydrogen bonds between water molecule and Fn, and blocked the direct polar interactions between Fn and hydrophilic substrates (Fig. S8). As there were negligible stable binding sites, weak adsorption of Fn was observed on SAMs-OH (Fig. S6) and repeated adsorption and desorption were noticed (see the trajectory movies in Supporting Information). The above simulation results mechanistically revealed the adsorption behavior of Fn on the neutral surfaces, in which high adsorption amount of Fn were found on SAMs-CH_3 but much less Fn could be detected on SAMs-OH (Fig. 2).

Supplementary video related to this article can be found at https://doi.org/10.1016/j.bioactmat.2021.02.021

We also investigated the interactions between Fn-III$_{7\text{-}10}$ and SAMs with positive/negative charge (SAMs-NH_2 and SAMs-COOH) from the last 100 ns of the MD simulations. The results showed that electrostatic interactions accounted for a major portion of the interactions in both systems (Fig. 6A and B), while large number of indirect/direct polar interactions were found between Fn and charged substrates (Fig. 6C). On

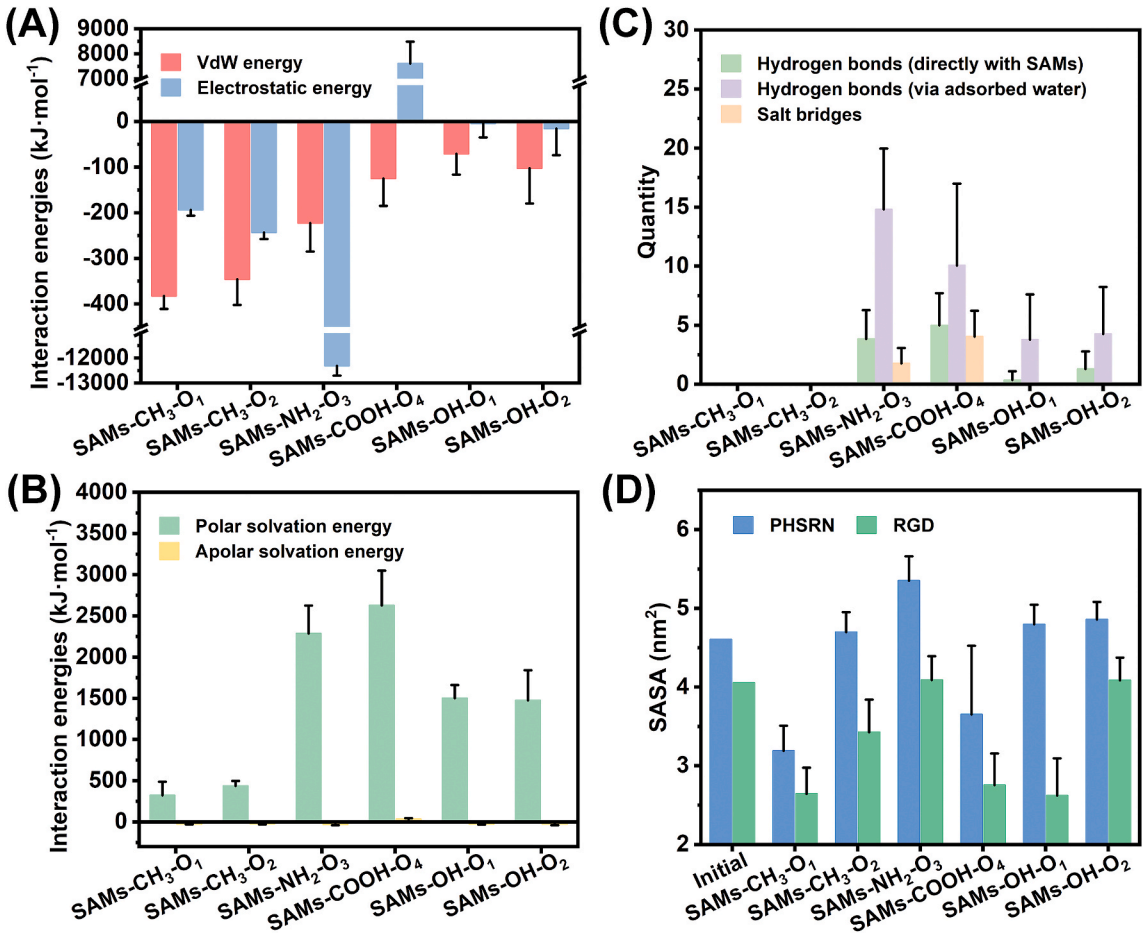

Fig. 6. Analysis of the last 100 ns of the MD simulations. (A) Intermolecular mechanical energies in terms of electrostatic interactions and van der Waals interactions and (B) polar/apolar solvation energies between Fn-III$_{7\text{-}10}$ and the indicated surfaces. (C) Intermolecular hydrogen bonds (directly or via adsorbed water molecules) and salt bridges between Fn-III$_{7\text{-}10}$ and the indicated surfaces. (D) The solvent accessible surface area (SASA) of the PHSRN and RGD motifs of Fn-III$_{7\text{-}10}$. Initial data were measured from the crystal structure of Fn-III$_{7\text{-}10}$.

SAMs-NH_2, the polar interactions led to a close binding of the "side-on" orientation of Fn. Specifically, Fn-III$_{7\text{-}8}$ preferably bound to SAMs-NH_2, since the protein domains had gradually reduced negative charge from Fn-III$_7$ to Fn-III$_{10}$ and the negative charge concentrated in Fn-III$_{7\text{-}8}$. However, there were mainly indirect polar interactions between Fn and the water layer on SAMs-NH_2, and these water-bridged hydrogen bonds would somehow block further direct interactions of Fn with the substrate. However, some salt bridges were formed, especially the one spotted between the carboxyl group of Glu^{1192} and the amino group of SAMs-NH_2, leading to a semi-direct binding of Fn eventually. Additionally, the effects of salt bridges were more evident on SAMs-COOH. As the electrostatic interactions, Fn would be repelled by SAMs-COOH, and the high positive polar solvation energy also indicated this phenomenon (Fig. 6A and B). However, nearly neutral domains, Fn-III$_9$ and Fn-III$_{10}$, managed to adsorb onto the SAMs-COOH through local distribution of the positively charged area on them. Many salt bridges were observed between the nitrogen atoms in the side chain of basic residues, e.g., Arg^{1379}, Arg^{1445}, and Lys^{1469}, and the carboxyl oxygen atoms of SAMs-COOH (Fig. S7), demonstrating strong direct interactions (Fig. 6C). As salt bridges had higher energy (approximately 4–8 k_BT [51]) than plain hydrogen bonds, they would theoretically be the major interactions to result in the stable adsorption of Fn on SAMs-NH_2 and SAMs-COOH, being consistent with the experimental results.

We further investigated the conformation of Fn on SAMs. The results showed that on different substrates, the RMSD of the protein fragment changed drastically, while that of each domain kept stable (Fig. S10B). By superimposing the protein structures (Fig. S9), we could also observe this phenomenon that the interdomain peptides between adjacent domains changed considerably but the structure of antiparallel β-sheet layers are largely retained in each domain. To quantify the variation, the interdomain angles between adjacent two domains were measured (Fig. S10C). These interdomain angles showed similar variation trends to those of the RMSD of the whole Fn-III$_{7\text{-}10}$, especially that ω_3 (the angle between Fn-III$_9$ and Fn-III$_{10}$) exhibited the significant contribution to the interdomain twist of Fn structure. Notably, on SAMs-CH_3, some changes could be observed inside the domain, being much more obvious than those on hydrophilic surfaces (Fig. S11). Specifically, there were deformations of reduced β-sheet and increased arbitrary coil in Fn-III$_7$ and Fn-III$_{10}$ on SAMs-CH_3, demonstrating the strong impact of the hydrophobic substrate on the binding domains. Additionally, the deformations would initiate larger hydrophobic area in Fn to interact with SAMs-CH_3 and significantly improve the adsorption efficiency as implied by the K_D value (Fig. 2).

The simulation results further explained the differences in Fn bioactivities. As mentioned above, SAM-CH_3 would break the ordered β-sheet layers and increase the arbitrary coil in the secondary structure of Fn-III$_7$ and Fn-III$_{10}$ (Fig. S11). The loss of β-sheet in Fn-III$_{10}$ would impact the local topology of RGD, reducing the bioactivities of Fn [52]. Additionally, on SAMs-CH_3, the RGD and PHSRN motifs in Fn-III$_{9\text{-}10}$ displayed reduced solvent accessible surface area (SASA) (Fig. 6D). As reported, RGD and PHSRN are the two main cell binding sites in Fn, which can independently initiate the binding of Fn with specific integrin receptors and induce osteogenic differentiation and calcium deposition [53,54]. Meanwhile, SASA is an important determinant of the

bioactivity of the protein/peptide on the surface, wherein a small SASA demonstrates a shielding of the residue and its bioactivity [55]. On SAMs-NH_2, Fn-III_{7-8} preferably bound to the surface (Fig.5D and Fig. S6) and raised the cell-binding domains in Fn-III_{9-10} to be away from substrate. Therefore, the RGD and PHSRN displayed large SASA, demonstrating the exposure of these residues to show high bioactivity. Conversely, Fn-III_{9-10} preferably adsorbed onto SAMs-COOH due to less negative charge, and both cell-binding sequences closed to the local positively charged region on Fn-III_{9-10} showed smaller SASA. Meanwhile, a newly formed intramolecular hydrogen bond around RGD motif was observed on SAMs-COOH (Fig. S12), which would further impact the bioactivity. However, the Fn on SAMs-COOH exhibited bioactivity. It was likely to be because that this Fn-III_{7-10} model lacked the complementary domains initiating the binding with heparin (Fn-I_{1-5} and Fn-III_{14-16}), collagen (Fn-I_{6-9}) and fibrin (Fn-I_{1-5} and Fn-I_{10-12}) outside the Fn-III_{7-10}, which could also mediate cell adhesion [56–58]. For SAMs-OH, although the SASA of RGD in Fn was smaller than those of SAMs-NH_2 and SAMs-COOH, the SASA of PHSRN was large. Additionally, the instability of the Fn adsorption would lead to large degree of protein flexibility. These factors should lead to the non-negligible bioactivity of Fn on SAMs-OH for cell proliferation, as shown in Fig. 3.

According to the above results, we summarized the relationship between surface charge/wettability and other properties (Fig. 7). Generally, the hydrophobic surface (SAMs-CH_3) could strongly adsorb proteins mainly by hydrophobic interactions. Most of the time, these hydrophobic interactions were strong due to the large hydrophobic area in the proteins partly resulting from structural rearrangement [43]. However, Fn on SAMs-CH_3 showed poor cell proliferation promotion calculated by quadratic fitting functions, integrin β_1 expression and osteogenic differentiation bioactivities. These should be caused by the low SASA of the RGD and PHSRN motifs and the deformation of the protein. Conversely, for the hydrophilic surface, both SAMs-NH_2 and SAMs-COOH could enhance the adsorption of Fn. Fn on SAMs-NH_2 exhibited excellent bioactivity that enhanced cell proliferation, integrin β_1 expression and osteogenic differentiation due to the high SASA of the bioactive sites (RGD and PHSRN). And although Fn on SAMs-COOH showed small SASA of RGD and PHSRN, the activation of other inferior cell-binding motifs might rescue the bioactivity. Additionally, as a water film forms on the non-charged hydrophilic surface of SAMs-OH, Fn would preferentially interact with water molecules instead of the substrates, resulting in the unstable binding of Fn. However, the small amount of Fn adsorbed on SAMs-OH would not be neglected because of the large SASA of PHSRN and the high protein flexibility.

Mechanistically revealing the relationship between biomaterial surface and the conformation/bioactivity of Fn was significant for rational design of Fn-activating biomaterials. To overcome this problem, researchers have employed simulations to study the behavior of Fn on the substrates on molecular scale, and some of them further combined experimental strategies [16,23,59–61]. However, most of these reports focused on single MC or MD simulation strategy. The single MC simulation was difficult to observe the thermodynamical changes in protein during adsorption [59], while the single plain MD simulation would be lack of optimized initial orientation of protein and the protein was easy to be trapped in the potential well [23,60,61]. These limitations would cause the loss of many significant data during simulation, and lead to the mismatching between simulation and experiment. In our research, we employed MC simulation to optimize the initial orientation of Fn and used all-atom MD simulation to demonstrate its behavior on surface. As the combination of MC and MD simulation, we found the unrevealed change of Fn conformation, e.g., the "end-on" orientation on SAMs-COOH. Additionally, we combined the experimental strategies to explain the Fn adsorption behavior, and especially the bioactivity of Fn to *hBMSCs* on molecular scale. As the improvement of the simulation strategies and the close combination of simulation/experiment, our results should be much more reasonable to explain the mechanism of Fn on the substrates.

Above all, we demonstrated the adsorption and bioactivity of Fn on different SAMs, and employed MC and MD simulations to reveal the mechanisms of the differences on the molecular scale. We believe that our results will have great potential for the rational design of Fn-activating biomaterials in the clinic.

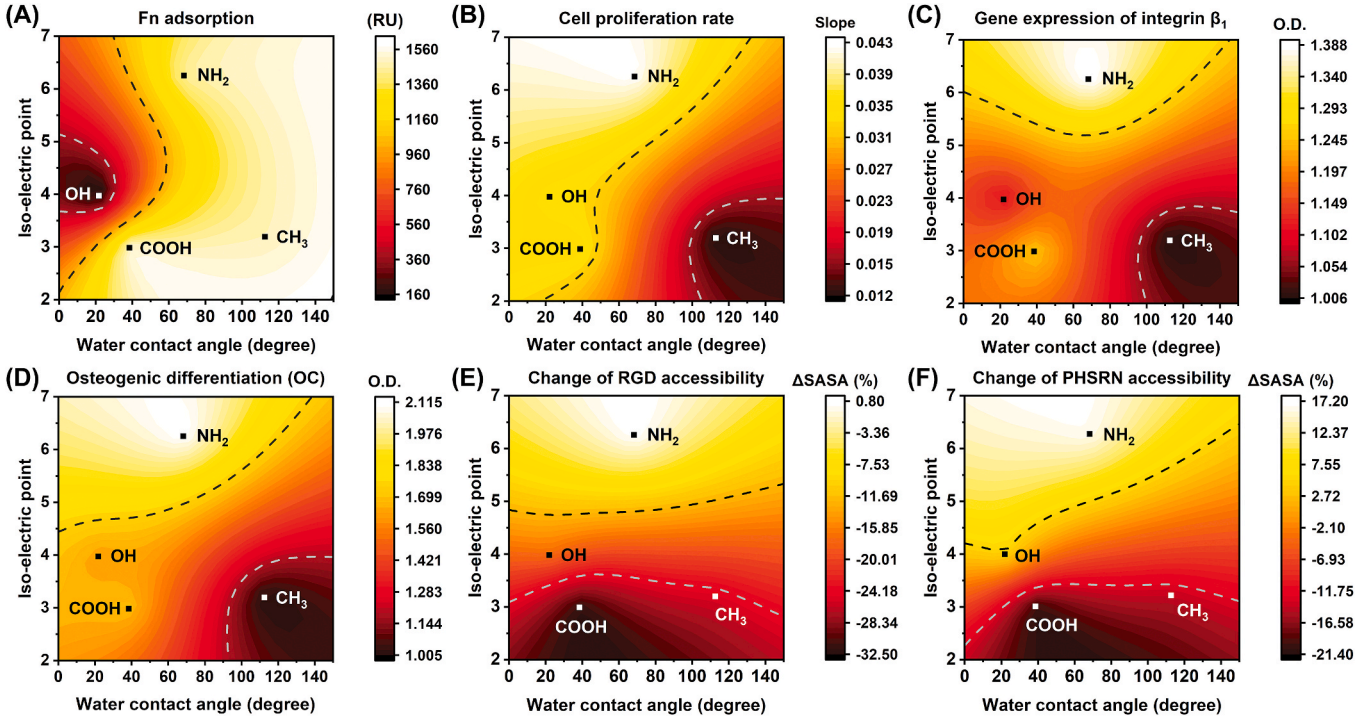

Fig. 7. The relationship between wettability/charge of the surfaces and the indicated property. (A) Fn adsorption. (B) Cell proliferation rate. (C) Gene expression of integrin β_1. (D) Osteogenic differentiation. (E) SASA of the RGD motif. (F) SASA of the PHSRN motif.

4. Conclusions

In summary, we characterized the Fn adsorption and subsequent cell behaviors on SAM substrates with different chemistries, i.e., SAMs-CH_3, SAMs-NH_2, SAMs-COOH and SAMs-OH. We revealed the mechanism of the difference according to the orientation and conformation of Fn on these surfaces on molecular scale by combining MC and all-atoms MD simulations. The results showed that Fn could strongly adsorb onto the hydrophobic surface of SAMs-CH_3 via hydrophobic interactions but showed poor bioactivity due to small SASA of RGD and PHSRN motifs and the deformation of the protein. Meanwhile, SAMs-NH_2 and SAMs-COOH could adsorb Fn efficiently via vdW interactions, electrostatic interactions, hydrogen bonds and salt bridges. Fn exhibited excellent bioactivity for cell adhesion, proliferation and osteogenic differentiation as high exposure of bioactive motifs on SAMs-NH_2, or as the activation of other inferior cell-binding motifs on SAMs-COOH. SAMs-OH showed poor Fn adsorption as the water film. Additionally, Fn was difficult to adhere on SAMs-OH due to the water film on the substrate, but the adsorbed Fn on SAMs-OH showed non-negligible bioactivity due to the large SASA of PHSRN and high protein flexibility. Our work provides a robust strategy to reveal the mechanism of interaction between the protein and the biomaterial surface through the combination of experimental strategies and molecular simulations. We believe that the mechanism revealed in this manuscript will be of great significance for the rational design of novel Fn-activating biomaterials in the clinic.

CRediT authorship contribution statement

Lijing Hao: Conceptualization, Methodology, Investigation, Writing – original draft, Data curation. **Tianjie Li:** Methodology, Investigation, Writing – original draft. **Lin Wang:** Conceptualization, Formal analysis, Investigation, Writing – review & editing. **Xuetao Shi:** Formal analysis, Writing – review & editing. **Yan Fan:** Methodology, Investigation. **Chang Du:** Methodology, Supervision, Writing – review & editing. **Yingjun Wang:** Conceptualization, Writing – review & editing, Supervision, Project administration.

Acknowledgements

This work was financially supported by National key R&D Program of China (2018YFC1105402, 2017YFC1104402, 2017YFC1105000), National Natural Science Foundation of China (31700823, U1801252, 31771027), Natural Science Foundation of Guangdong Province of China (2020A1515011354, 2017A030310335), Science and Technology Program of Guangzhou (201804020060), the Guangdong Natural Science Funds for Distinguished Young Scholars (2019B151502029), the Pearl River Nova Program of Guangzhou (201806010156), Outstanding Scholar Program of Guangzhou Regenerative Medicine and Health Guangdong Laboratory (2018GZR110102001) and the Fundamental Research Funds for the Central Universities. L.W. thanks the Funds for Young Pearl River Scholars.

Appendix A. Supplementary data

Supplementary data to this article can be found online at https://doi.org/10.1016/j.bioactmat.2021.02.021.

References

[1] H. Chen, L. Yuan, W. Song, Z.K. Wu, D. Li, Biocompatible polymer materials: role of protein-surface interactions, Prog. Polym. Sci. 33 (2008) 1059–1087, https://doi.org/10.1016/j.progpolymsci.2008.07.006.

[2] J. Wang, X. Chen, B. Guo, X. Yang, Y. Zhou, X. Zhu, K. Zhang, Y. Fan, C. Tu, X. Zhang, A serum protein adsorption profile on BCP ceramics and influence of the elevated adsorption of adhesive proteins on the behaviour of MSCs, J. Mater. Chem. B 6 (2018) 7383–7395, https://doi.org/10.1039/c8tb02283f.

[3] M. Salmeron-Sanchez, P. Rico, D. Moratal, T.T. Lee, J.E. Schwarzbauer, A.J. Garcia, Role of material-driven fibronectin fibrillogenesis in cell differentiation, Biomaterials 32 (2011) 2099–2105, https://doi.org/10.1016/j.biomaterials.2010.11.057.

[4] M. Lin, S. Mao, J. Wang, J. Xing, Y. Wang, K. Cai, Y. Luo, Adsorption force of fibronectin controls transmission of cell traction force and subsequent stem cell fate, Biomaterials 162 (2018) 170–182, https://doi.org/10.1016/j.biomaterials.2018.01.036.

[5] L.I. Gold, E. Pearlstein, Fibronectin-collagen binding and requirement during cellular adhesion, Biochem. J. 186 (1980) 551–559, https://doi.org/10.1042/bj1860551.

[6] C.P. Jara, O. Wang, T. Paulino do Prado, A. Ismail, F.M. Fabian, H. Li, L.A. Velloso, M.A. Carlson, W. Burgess, Y. Lei, W.H. Velander, E.P. Araujo, Novel fibrin-fibronectin matrix accelerates mice skin wound healing, Bioact Mater 5 (2020) 949–962, https://doi.org/10.1016/j.bioactmat.2020.06.015.

[7] A.A. Dayem, J. Won, H.G. Goo, G.M. Yang, D.S. Seo, B.M. Jeon, H.Y. Choi, S. E. Park, K.M. Lim, S.H. Jang, S.B. Lee, S.B. Choi, K. Kim, G.H. Kang, G.B. Yeon, D. S. Kim, S.G. Cho, The immobilization of fibronectin- and fibroblast growth factor 2-derived peptides on a culture plate supports the attachment and proliferation of human pluripotent stem cells, Stem Cell Res. 43 (2020) 101700, https://doi.org/10.1016/j.scr.2020.101700.

[8] G. Efthymiou, A. Saint, M. Ruff, Z. Rekad, D. Ciais, E. Van Obberghen-Schilling, Shaping up the tumor microenvironment with cellular fibronectin, Front Oncol 10 (2020) 641, https://doi.org/10.3389/fonc.2020.00641.

[9] J.J. Sakon, K.R. Weninger, Detecting the conformation of individual proteins in live cells, Nat. Methods 7 (2010) 203–205, https://doi.org/10.1038/nmeth.1421.

[10] M. Obara, M.S. Kang, K.M. Yamada, Site-directed mutagenesis of the cell-binding domain of human fibronectin: separable, synergistic sites mediate adhesive function, Cell 53 (1988) 649–657, https://doi.org/10.1016/0092-8674(88)90580-6.

[11] H.R. Kwon, M. Larsen, The contribution of specific cell subpopulations to submandibular salivary gland branching morphogenesis, Curr. Opin. Genet. Dev. 32 (2015) 47–54, https://doi.org/10.1016/j.gde.2015.01.007.

[12] A. Dolatshahi-Pirouz, T. Jensen, D.C. Kraft, M. Foss, P. Kingshott, J.L. Hansen, A. N. Larsen, J. Chevallier, F. Besenbacher, Fibronectin adsorption, cell adhesion, and proliferation on nanostructured tantalum surfaces, ACS Nano 4 (2010) 2874–2882, https://doi.org/10.1021/nn9017872.

[13] M.A. Lan, C.A. Gersbach, K.E. Michael, B.G. Keselowsky, A.J. Garcia, Myoblast proliferation and differentiation on fibronectin-coated self assembled monolayers presenting different surface chemistries, Biomaterials 26 (2005) 4523–4531, https://doi.org/10.1016/j.biomaterials.2004.11.028.

[14] S.B. Kennedy, N.R. Washburn, C.G. Simon Jr., E.J. Amis, Combinatorial screen of the effect of surface energy on fibronectin-mediated osteoblast adhesion, spreading and proliferation, Biomaterials 27 (2006) 3817–3824, https://doi.org/10.1016/j.biomaterials.2006.02.044.

[15] L. Rouxhet, F. Duhoux, O. Borecky, R. Legras, Y.J. Schneider, Adsorption of albumin, collagen, and fibronectin on the surface of poly(hydroxybutyrate-hydroxyvalerate) (PHB/HV) and of poly (epsilon-caprolactone) (PCL) films modified by an alkaline hydrolysis and of poly(ethylene terephtalate) (PET) track-etched membranes, J. Biomater. Sci. Polym. Ed. 9 (1998) 1279–1304, https://doi.org/10.1163/156856298x00398.

[16] K.E. Michael, V.N. Vernekar, B.G. Keselowsky, J.C. Meredith, R.A. Latour, A. J. Garcia, Adsorption-induced conformational changes in fibronectin due to interactions with well-defined surface chemistries, Langmuir 19 (2003) 8033–8040, https://doi.org/10.1021/la034810a.

[17] J.R. Capadona, D.M. Collard, A.J. Garcia, Fibronectin adsorption and cell adhesion to mixed monolayers of tri(ethylene glycol)- and methyl-terminated alkanethiols, Langmuir 19 (2003) 1847–1852, https://doi.org/10.1021/la026244+.

[18] C.C. Barrias, M.C. Martins, G. Almeida-Porada, M.A. Barbosa, P.L. Granja, The correlation between the adsorption of adhesive proteins and cell behaviour on hydroxyl-methyl mixed self-assembled monolayers, Biomaterials 30 (2009) 307–316, https://doi.org/10.1016/j.biomaterials.2008.09.048.

[19] K. Anselme, A. Ponche, M. Bigerelle, Relative influence of surface topography and surface chemistry on cell response to bone implant materials. Part 2: biological aspects, Proc. Inst. Mech. Eng. H 224 (2010) 1487–1507, https://doi.org/10.1243/09544119JEIM901.

[20] B.G. Keselowsky, D.M. Collard, A.J. Garcia, Surface chemistry modulates fibronectin conformation and directs integrin binding and specificity to control cell adhesion, J. Biomed. Mater. Res. 66 (2003) 247–259, https://doi.org/10.1002/jbm.a.10537.

[21] L. Lv, K. Li, Y. Xie, Y. Cao, X. Zheng, Enhanced osteogenic activity of anatase TiO2 film: surface hydroxyl groups induce conformational changes in fibronectin, Mater Sci Eng C Mater Biol Appl 78 (2017) 96–104, https://doi.org/10.1016/j.msec.2017.04.056.

[22] T. Li, L. Hao, J. Li, C. Du, Y. Wang, Insight into vitronectin structural evolution on material surface chemistries: the mediation for cell adhesion, Bioact Mater 5 (2020) 1044–1052, https://doi.org/10.1016/j.bioactmat.2020.06.021.

[23] K. Wilson, S.J. Stuart, A. Garcia, R.A. Latour Jr., A molecular modeling study of the effect of surface chemistry on the adsorption of a fibronectin fragment spanning the 7-10th type III repeats, J. Biomed. Mater. Res. 69 (2004) 686–698, https://doi.org/10.1002/jbm.a.30042.

[24] J. Zhou, S.F. Chen, S.Y. Jiang, Orientation of adsorbed antibodies on charged surfaces by computer simulation based on a united-residue model, Langmuir 19 (2003) 3472–3478, https://doi.org/10.1021/la026871z.

[25] J. Zhou, J. Zheng, S.Y. Jiang, Molecular simulation studies of the orientation and conformation of cytochrome c adsorbed on self-assembled monolayers, J. Phys. Chem. B 108 (2004) 17418–17424, https://doi.org/10.1021/jp038048x.

[26] M. Abraham, D. Van Der Spoel, E. Lindahl, B. Hess, The GROMACS Development Team, GROMACS User Manual Version 5.0.7, 2015, p. 5.
[27] K. Vanommeslaeghe, E. Hatcher, C. Acharya, S. Kundu, S. Zhong, J. Shim, E. Darian, O. Guvench, P. Lopes, I. Vorobyov, A.D. Mackerell Jr., CHARMM general force field: a force field for drug-like molecules compatible with the CHARMM all-atom additive biological force fields, J. Comput. Chem. 31 (2010) 671–690, https://doi.org/10.1002/jcc.21367.
[28] A.D. MacKerell, D. Bashford, M. Bellott, R.L. Dunbrack, J.D. Evanseck, M.J. Field, S. Fischer, J. Gao, H. Guo, S. Ha, D. Joseph-McCarthy, L. Kuchnir, K. Kuczera, F. T. Lau, C. Mattos, S. Michnick, T. Ngo, D.T. Nguyen, B. Prodhom, W.E. Reiher, B. Roux, M. Schlenkrich, J.C. Smith, R. Stote, J. Straub, M. Watanabe, J. Wiorkiewicz-Kuczera, D. Yin, M. Karplus, All-atom empirical potential for molecular modeling and dynamics studies of proteins, J. Phys. Chem. B 102 (1998) 3586–3616, https://doi.org/10.1021/jp973084f.
[29] W. Yu, X. He, K. Vanommeslaeghe, A.D. MacKerell Jr., Extension of the CHARMM General Force Field to sulfonyl-containing compounds and its utility in biomolecular simulations, J. Comput. Chem. 33 (2012) 2451–2468, https://doi.org/10.1002/jcc.23067.
[30] W.L. Jorgensen, J. Chandrasekhar, J.D. Madura, R.W. Impey, M.L. Klein, Comparison of simple potential functions for simulating liquid water, J. Chem. Phys. 79 (1983) 926–935, https://doi.org/10.1063/1.445869.
[31] W.G. Hoover, Canonical dynamics: equilibrium phase-space distributions, Phys Rev A Gen Phys 31 (1985) 1695–1697, https://doi.org/10.1103/physreva.31.1695.
[32] B. Hess, H. Bekker, H.J.C. Berendsen, J.G.E.M. Fraaije, LINCS: a linear constraint solver for molecular simulations, J. Comput. Chem. 18 (1997) 1463–1472, https://doi.org/10.1002/(Sici)1096-987x(199709)18:12<1463::Aid-Jcc4>3.3.Co;2-L.
[33] T. Darden, D. York, L. Pedersen, Particle mesh Ewald - an N.log(N) method for Ewald sums in large systems, J. Chem. Phys. 98 (1993) 10089–10092, https://doi.org/10.1063/1.464397.
[34] W. Humphrey, A. Dalke, K. Schulten, VMD: visual molecular dynamics, J. Mol. Graph. 14 (33–8) (1996) 27–28, https://doi.org/10.1016/0263-7855(96)00018-5.
[35] N.A. Baker, D. Sept, S. Joseph, M.J. Holst, J.A. McCammon, Electrostatics of nanosystems: application to microtubules and the ribosome, Proc. Natl. Acad. Sci. Unit. States Am. 98 (2001) 10037–10041, https://doi.org/10.1073/pnas.181342398.
[36] R. Kumari, R. Kumar, A. Lynn, g_mmpbsa—a GROMACS tool for high-throughput MM-PBSA calculations, J. Chem. Inf. Model. 54 (2014) 1951–1962, https://doi.org/10.1021/ci500020m.
[37] L.L.C. Schrodinger, The PyMOL Molecular Graphics System, 2015, Version 2.0.
[38] W. Kabsch, C. Sander, Dictionary of protein secondary structure: pattern recognition of hydrogen-bonded and geometrical features, Biopolymers 22 (1983) 2577–2637, https://doi.org/10.1002/bip.360221211.
[39] W.G. Touw, C. Baakman, J. Black, T.A. te Beek, E. Krieger, R.P. Joosten, G. Vriend, A series of PDB-related databanks for everyday needs, Nucleic Acids Res. 43 (2015) D364–D368, https://doi.org/10.1093/nar/gku1028.
[40] L. Hao, T. Li, F. Yang, N. Zhao, F. Cui, X. Shi, C. Du, Y. Wang, The correlation between osteopontin adsorption and cell adhesion to mixed self-assembled monolayers of varying charges and wettability, Biomater Sci 5 (2017) 800–807, https://doi.org/10.1039/c6bm00802j.
[41] L. Hao, H. Yang, C. Du, X. Fu, N. Zhao, S. Xu, F. Cui, C. Mao, Y. Wang, Directing the fate of human and mouse mesenchymal stem cells by hydroxyl-methyl mixed self-assembled monolayers with varying wettability, J. Mater. Chem. B 2 (2014) 4794–4801, https://doi.org/10.1039/C4TB00597J.
[42] L. Hao, X. Fu, T. Li, N. Zhao, X. Shi, F. Cui, C. Du, Y. Wang, Surface chemistry from wettability and charge for the control of mesenchymal stem cell fate through self-assembled monolayers, Colloids Surf. B Biointerfaces 148 (2016) 549–556, https://doi.org/10.1016/j.colsurfb.2016.09.027.
[43] M.J. Penna, M. Mijajlovic, M.J. Biggs, Molecular-level understanding of protein adsorption at the interface between water and a strongly interacting uncharged solid surface, J. Am. Chem. Soc. 136 (2014) 5323–5331, https://doi.org/10.1021/ja411796e.
[44] Z. Wang, Z. Cheng, V. Singh, Z. Zheng, Y. Wang, S. Li, L. Song, J. Zhu, Stable and sensitive silver surface plasmon resonance imaging sensor using trilayered metallic structures, Anal. Chem. 86 (2014) 1430–1436, https://doi.org/10.1021/ac402126k.
[45] F.G. Giancotti, E. Ruoslahti, Integrin signaling, Science 285 (1999) 1028–1032, https://doi.org/10.1126/science.285.5430.1028.
[46] G.M. Boland, G. Perkins, D.J. Hall, R.S. Tuan, Wnt 3a promotes proliferation and suppresses osteogenic differentiation of adult human mesenchymal stem cells, J. Cell. Biochem. 93 (2004) 1210–1230, https://doi.org/10.1002/jcb.20284.
[47] Y.J. Kim, Y.C. Bae, K.T. Suh, J.S. Jung, Quercetin, a flavonoid, inhibits proliferation and increases osteogenic differentiation in human adipose stromal cells, Biochem. Pharmacol. 72 (2006) 1268–1278, https://doi.org/10.1016/j.bcp.2006.08.021.
[48] Y. Kang, A.I. Georgiou, R.J. MacFarlane, M.E. Klontzas, M. Heliotis, E. Tsiridis, A. Mantalaris, Fibronectin stimulates the osteogenic differentiation of murine embryonic stem cells, J Tissue Eng Regen Med 11 (2017) 1929–1940, https://doi.org/10.1002/term.2090.
[49] R. McBeath, D.M. Pirone, C.M. Nelson, K. Bhadriraju, C.S. Chen, Cell shape, cytoskeletal tension, and RhoA regulate stem cell lineage commitment, Dev. Cell 6 (2004) 483–495, https://doi.org/10.1016/s1534-5807(04)00075-9.
[50] A.J. Engler, S. Sen, H.L. Sweeney, D.E. Discher, Matrix elasticity directs stem cell lineage specification, Cell 126 (2006) 677–689, https://doi.org/10.1016/j.cell.2006.06.044.
[51] H. Gohlke, G. Klebe, Approaches to the description and prediction of the binding affinity of small-molecule ligands to macromolecular receptors, Angew Chem. Int. Ed. Engl. 41 (2002) 2644–2676, https://doi.org/10.1002/1521-3773(20020802)41:15<2644::AID-ANIE2644>3.0.CO;2-O.
[52] L. Baugh, V. Vogel, Structural changes of fibronectin adsorbed to model surfaces probed by fluorescence resonance energy transfer, J. Biomed. Mater. Res. 69 (2004) 525–534, https://doi.org/10.1002/jbm.a.30026.
[53] H. Bachman, J. Nicosia, M. Dysart, T.H. Barker, Utilizing fibronectin integrin-binding specificity to control cellular responses, Adv. Wound Care 4 (2015) 501–511, https://doi.org/10.1089/wound.2014.0621.
[54] P. Dhavalikar, A. Robinson, Z. Lan, D. Jenkins, M. Chwatko, K. Salhadar, A. Jose, R. Kar, E. Shoga, A. Kannapiran, E. Cosgriff-Hernandez, Review of integrin-targeting biomaterials in tissue engineering, Adv Healthc Mater (2020), e2000795, https://doi.org/10.1002/adhm.202000795 n/a.
[55] L. Wang, J. Chen, X. Zeng, P.P. Cheung, X. Zheng, L. Xie, X. Shi, L. Ren, X. Huang, Y. Wang, Mechanistic insights and rational design of a versatile surface with cells/bacteria recognition capability via orientated fusion peptides, Adv. Sci. 6 (2019) 1801827, https://doi.org/10.1002/advs.201801827.
[56] J.V. Moyano, A. Maqueda, B. Casanova, A. Garcia-Pardo, Alpha4beta1 integrin/ligand interaction inhibits alpha5beta1-induced stress fibers and focal adhesions via down-regulation of RhoA and induces melanoma cell migration, Mol. Biol. Cell 14 (2003) 3699–3715, https://doi.org/10.1091/mbc.e02-10-0667.
[57] R.J. Owens, F.E. Baralle, Mapping the collagen-binding site of human fibronectin by expression in Escherichia coli, EMBO J. 5 (1986) 2825–2830, https://doi.org/10.1002/j.1460-2075.1986.tb04575.x.
[58] A. Sharma, J.A. Askari, M.J. Humphries, E.Y. Jones, D.I. Stuart, Crystal structure of a heparin- and integrin-binding segment of human fibronectin, EMBO J. 18 (1999) 1468–1479, https://doi.org/10.1093/emboj/18.6.1468.
[59] H. Wang, Y. He, B.D. Ratner, S. Jiang, Modulating cell adhesion and spreading by control of FnIII7-10 orientation on charged self-assembled monolayers (SAMs) of alkanethiolates, J. Biomed. Mater. Res. 77 (2006) 672–678, https://doi.org/10.1002/jbm.a.30586.
[60] E. Liamas, K. Kubiak-Ossowska, R.A. Black, O.R.T. Thomas, Z.J. Zhang, P. A. Mulheran, Adsorption of fibronectin fragment on surfaces using fully atomistic molecular dynamics simulations, Int. J. Mol. Sci. 19 (2018), https://doi.org/10.3390/ijms19113321.
[61] M. Panos, T.Z. Sen, M.G. Ahunbay, Molecular simulation of fibronectin adsorption onto polyurethane surfaces, Langmuir 28 (2012) 12619–12628, https://doi.org/10.1021/la301546v.